Microporous and Mesoporous Materials 333 (2022) 111665

Contents lists available at ScienceDirect

Microporous and Mesoporous Materials

journal homepage: www.elsevier.com/locate/micromeso

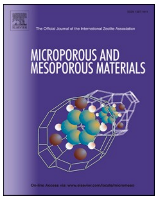

Hosting $AlCl_3$ on ternary metal oxide composites for catalytic oligomerization of 1-decene: Revealing the role of supports via performance evaluation and DFT calculation

Yue Lou[a], Yuxiang Chen[a], Yang Zhao[a], Cheng Qian[a], Cheng Niu[a], Hao Jiang[a], Chuanlei Liu[a], Kongguo Wu[a], Benxian Shen[a,b], Jian Long[c,*], Yiming Wang[a,**], Hui Sun[a,b,***], Jigang Zhao[a,b], Jichang Liu[a,b], Hao Ling[a,b], Di Wu[d,e,f,g], Yujun Tong[h]

[a] *School of Chemical Engineering, East China University of Science and Technology, Shanghai, 200237, China*
[b] *International Joint Research Center of Green Energy Chemical Engineering, East China University of Science and Technology, Shanghai, 200237, China*
[c] *Key Laboratory of Smart Manufacturing in Energy Chemical Process, Ministry of Education, East China University of Science and Technology, Shanghai 200237, China*
[d] *Alexandra Navrotsky Institute for Experimental Thermodynamics, Washington State University, Pullman, WA, 99163, United States*
[e] *The Gene and Linda Voiland School of Chemical Engineering and Bioengineering, Washington State University, Pullman, WA, 99163, United States*
[f] *Department of Chemistry, Washington State University, Pullman, WA, 99163, United States*
[g] *Materials Science and Engineering, Washington State University, Pullman, WA, 99163, United States*
[h] *Sinopec Dalian Research Institute of Petroleum and Petrochemicals, Dalian Liaoning, 116100, China*

ARTICLE INFO

Keywords:
Activity
Stability
1-Decene oligomerization
Immobilization
Host-guest interaction

ABSTRACT

Enhancing catalytic activity and stability of supported Lewis acid catalysts remain a particular challenge owing to the limited understanding and unsatisfactory tuning of the interplay between the active components and the supports. Herein, upon immobilizing $AlCl_3$ on a series of ternary metal oxides including La_2O_3–Al_2O_3–SiO_2, NiO–Al_2O_3–SiO_2 and Ga_2O_3–Al_2O_3–SiO_2, we clearly revealed the influence of the compositions and structures of the supports on the catalyst performances through experiments together with density functional theory (DFT) calculations. The catalytic performances of the supported samples were evaluated by oligomerization of 1-decene using both batch reactor and fixed-bed apparatus. The results suggest that the $AlCl_3$ supported by NiO–Al_2O_3–SiO_2 composites exhibits the highest catalytic activity and stability because of its positive pore structure and thereof the high loading of active species. Importantly, DFT calculations indicate that the variations of the host-guest interaction energy between the ternary oxide composites and $AlCl_3$ are in good agreement with the experimental results. This study highlights the compositions and structures of the supports are crucial to the catalytic performances of Lewis acid catalysts, and provides fundamental guidance for design of high-performance supported catalysts.

1. Introduction

In recent years, in view of increasing concerns with regard to environmental and industrial sustainability, high-performance, green and renewable catalysts for production of chemicals are highly desired [1–3]. Lewis acids as a class of important catalysts have been widely used in a variety of reactions, such as Friedel-Crafts [4–6], methylation [7], alkylation [8] and olefin polymerization [9]. Generally, the products synthesized by direct employment of pure active species need further treatments including catalyst separation, neutralization, water washing and thorough removal of ionic species, which usually lead to both environmental issues and economic concerns.

To address the aforementioned problems, many efforts have been made in recent years to host active species on functionalized supports with the aim to realize the sustainable industrial applications of Lewis acid catalysts [10–12]. For instance, tremendous porous materials such

---

[*] Corresponding author. Key Laboratory of Smart Manufacturing in Energy Chemical Process, Ministry of Education, East China University of Science and Technology, Shanghai 200237, China.

[**] Corresponding author. School of Chemical Engineering, East China University of Science and Technology, Shanghai, 200237, China.

[***] Corresponding author. School of Chemical Engineering, East China University of Science and Technology, Shanghai, 200237, China.

E-mail addresses: longjian@ecust.edu.cn (J. Long), yimingwang@ecust.edu.cn (Y. Wang), sunhui@ecust.edu.cn (H. Sun).

https://doi.org/10.1016/j.micromeso.2021.111665
Received 14 October 2021; Received in revised form 5 December 2021; Accepted 27 December 2021

as silica gel [13], activated carbon [14], montmorillonite [15], molecular sieve [16], graphite [17], polystyrene [18], activated alumina [19] have been developed and used as supports of $AlCl_3$, one of the most extensively used Lewis acid catalysts in various chemical conversions. As an important example, polyalphaolefin (PAO), a widely used lubricant base oil, is commonly synthesized by $AlCl_3$ catalyzed oligomerization of linear α-olefins [20–22]. To develop environment-friendly PAO production process, recyclable immobilized catalysts therefore has been of great interests [21]. For example, a supported catalyst was prepared via loading $AlCl_3$ on γ-Al_2O_3 using impregnation method and $NiSO_4$ as co-catalyst for continuous oligomerization in a fixed-bed reactor [23]. In another example, SiO_2 was used as a support of $AlCl_3$ for catalytic oligomerization of 1-decene [24]. In previous work, we also prepared a number of supported catalysts by the impregnation of bimetallic components of $AlCl_3$ and $TiCl_4$ onto different supports including activated carbon, γ-Al_2O_3, molecular sieves and silica gel [25]. Very recently, we synthesized a series of ternary oxide composites ($MgO–Al_2O_3–SiO_2$) with different Si/Al ratios and used them as supports to host active components of $AlCl_3$ and $TiCl_4$, leading to much higher activity and stability of supported catalysts as compared to those derived from monoxide [26]. However, immobilized $AlCl_3$ catalysts remain to suffer from active sites reduction and inevitable deactivation. Furthermore, our previous findings indicated that the immobilization of active species and stability of supported catalysts strongly depended on the chemical compositions and structures of porous host architectures. The escape of active components from supports can be attributed to the weak host-guest interactions. Therefore, unveiling the host-guest interactions between the supports and active components and unlocking the relationship between the properties of supports and the catalytic performances of catalysts are fundamentally important, which can provide guidance for the design of preferable supports enabling the immobilized catalysts to show outstanding catalytic activity and stability.

Herein, with a focus on the oligomerization of 1-decene, we systematically investigated the effects of compositions as well as structures of supports on the catalytic performances of $AlCl_3$, thereon revealed the underlying effect mechanism from host-guest interactions between supports and $AlCl_3$ combing with density functional theory (DFT) calculations. In the preparation of supports, we employed different metals, including lanthanide metals, transition metals, and post-transition metals, in order to understand the roles of metal in determining the host-guest interactions between the supports and active components. The supported catalysts were prepared by impregnating $AlCl_3$ on a series of ternary metal oxide composites under different conditions. All the supports and resulting supported catalysts were carefully characterized to examine their structural changes. The catalytic activity and stability of the supported catalysts for the oligomerization of 1-decene were tested in a batch reactor and a custom-made fixed-bed reactor, respectively. In addition, the host-guest interactions between different supports and $AlCl_3$ were investigated by DFT calculations. The present study highlights the crucial dependence of the catalytic performances of immobilized Lewis acid catalysts on the structures and compositions of the supports, offering a fundamental rule for the rational design of effective supported catalysts.

2. Experimental methods

2.1. Materials and reagents

Aluminum nitrate hydrate, magnesium nitrate hydrate, lanthanum nitrate hydrate, nickel nitrate hydrate, gallium nitrate hydrate and nitric acid were provided by Sinopharm Chemical Reagent Co., Ltd., China. All of these chemicals are of >99% purity except for the nitric acid with a concentration of 68%. Silica sol (having solid content of 30% and colloidal particle diameter of 10–20 nm) was obtained from Qingdao Mike Silica Gel Desiccant Co., Ltd., China. Both anhydrous aluminum trichloride (purity >98%) and carbon tetrachloride (purity >99%) were provided by Shanghai Titan Scientific Co., Ltd., China. And 1-decene (purity >97%) was supplied by Shanghai Moen Chemical Technology Co., Ltd., China.

2.2. Preparation of the supports and the supported catalysts

The same method described in our earlier work [26] was employed to prepare the supports and the supported catalysts. $MgO–Al_2O_3–SiO_2$ support was prepared and its derived catalyst was used as a reference. A general preparation process is illustrated in Scheme S1. Firstly, 41.7 g of aluminum nitrate hydrate and 59.9 g of lanthanum nitrate hydrate were thoroughly dissolved in a solution (mixing 2.4 g nitric acid with 200 g deionized water). Then 471.6 g silica sol was added into former solution under stirring at room temperature (RT) and the mixture was stirred for more than 2 h to obtain a slurry precursor. After that, the resulting mixture was heated at 50 °C for 24 h to form a gel. Finally, the $La_2O_3–Al_2O_3–SiO_2$ support can be obtained through dehydration at 150 °C in an oven, trituration and sieving to 10–20 mesh particle size. By replacing lanthanum nitrate hydrate with nickel nitrate hydrate or gallium nitrate hydrate, different metal oxides can be introduced into the supports. Prior to the immobilization of $AlCl_3$, all the resultant supports undergo the following thermal treatment procedure: heating the samples to two temperature plateaus of 300 °C and 600 °C, respectively at 3 °C/min, and holding each of the plateau temperature for 3 h.

The supported catalysts were prepared by loading $AlCl_3$ onto above-synthesized ternary oxide composites. All immobilization experiments were carried out using carbon tetrachloride as the solvent. All supported catalysts were prepared by referring to the procedure reported in our previous work [25,26]. The specific preparation process was performed using a three-port flask reactor. Prior to immobilization, the reactor was purged with nitrogen for about 10 min to remove moisture. 150 mL of carbon tetrachloride, 30 g of synthesized supports and 12 g of anhydrous aluminum chloride were added to the reactor. Then immobilization was realized through performing a reflux process at 80 °C for 12 h under magnetic stirring. Hereafter, the immobilized catalyst was separated from the mixture by filtration and the residual solvent was removed using a nitrogen flow. The supports of $MgO–Al_2O_3–SiO_2$, $La_2O_3–Al_2O_3–SiO_2$, $NiO–Al_2O_3–SiO_2$, and $Ga_2O_3–Al_2O_3–SiO_2$ were denoted as S-1, S-2, S-3 and S-4, respectively. And their derived catalyst samples of $AlCl_3/MgO–Al_2O_3–SiO_2$, $AlCl_3/La_2O_3–Al_2O_3–SiO_2$, $AlCl_3/NiO–Al_2O_3–SiO_2$, and $AlCl_3/Ga_2O_3–Al_2O_3–SiO_2$ were labeled as M − 1, M − 2, M − 3, and M − 4 (see Tables S1 and S2 for detailed information), respectively.

2.3. Catalytic performance evaluation

Catalytic oligomerization of 1-decene was carried out in a batch reactor (See Fig. S1) to examine the activity of different catalysts. At first, catalyst sample and 1-decene were introduced into the reactor with a mass ratio of 1:4. The reaction was performed at 30 °C in N_2 atmosphere for 8 h with a stirring rate of 1800 r/min. After the reaction was finished, oligomerized product and the catalysts were separated for characterizations and tests.

Stability of catalyst was evaluated in a custom-made fixed-bed reactor with an inner diameter of 15 mm (See Fig. S2). 24 g supported catalyst was filled for each round of reaction. The catalyst was kept in the middle constant temperature section by filling quartz sand at both top and bottom of the reactor. Prior to the experiment, the apparatus was purged with nitrogen flow for 10 min to expel undesired gases. Once the bed temperature reached the desired value, 1-decene was fed from the top of the reactor and oligomerization product was collected at the bottom at different reaction time.

The yields of products, Y, were calculated using Equation (1):

$$Y(\%) = \frac{Wt}{W0} \times 100\% \tag{1}$$

where W_t is the mass of the >280 °C distillation in the oligomerization products and W_0 represents total mass of the raw materials.

2.4. Sample characterizations

The specific surface area and pore size distribution of the supports and catalysts were measured by N_2 adsorption at −196 °C using a Micromeritics ASAP 2010 physisorption analyzer. All samples were degassed at 300 °C for 5 h under vacuum and then measured in the pressure range of 0.4–101.8 kPa. Thermogravimetry analysis (TGA) was performed on a SDT Q600 system (TA Instruments, USA). Sample was placed in a platinum crucible and heated from RT to 800 °C at 10 °C/min under the oxygen flow (40 mL/min). X-ray photoelectron spectroscopy (XPS) analysis was carried out on a Thermo Scientific ESCALAB 250Xi spectrometer (Thermo Fisher Scientific, USA). The pyridine adsorption infrared (Py-IR) analysis was performed using a V70 Fourier infrared spectroscopy (Bruker, Germany). The powder sample was pressed into a 13 mm wafer, vacuum degassed at 300 °C for 2 h and cooled to 100 °C under dynamic vacuum to adsorb pyridine for 30 min. Thereafter, sample was heated using temperature-programmed method and desorbed at 150 °C and 400 °C, respectively.

S-4800 scanning electron microscope (Hitachi, Japan) was used to analyze the morphologies of the samples at a scan voltage of 3 kV. A transmission electron microscope (JEM-2100, JEOL) was also employed to observe the microscopic morphology using an accelerating voltage of 200 kV. All samples were prepared via ultrasonic dispersion in ethanol. A slow scan CCD camera was used to collect images. Elemental distributions in microscopic regions of the samples were evaluated using a Falcon energy-dispersive spectrometer (EDS) (EDAX Inc., USA).

The kinematic viscosity of PAO products was tested at 40 °C and 100 °C, denoted as v_{40} and v_{100}, respectively. The viscosity index (VI) can be derived from v_{40} and v_{100} according to ASTM D2270. Freezing point (FP) was measured using a SYP1022-2 freezing point analyzer (Shanghai Boli Instrument Co., Ltd., China). ZWC-2001 microcomputer salt content analyzer (Jiangsu Jierui Instrument and Equipment Co., Ltd., China) was used to determine the chlorine content of the supported catalyst. The catalyst sample weighing about 1 g was treated with 100 mL of 0.5 mol/L nitric acid solution for 10 h and washed with deionized water for least three times. The solution was collected by centrifugation and diluted to 500 mL with deionized water for chlorine content determination. According to $X_{Cl} = 500C_0/m_0$, the mass fraction of chlorine in catalyst sample can be calculated simply, where C_0 is the chlorine content in the solution, g/mL, and m_0 is the mass of the catalyst sample, g.

2.5. DFT calculations

The Vienna Ab initio Package (VASP) [27,28] was employed to perform all density functional theory (DFT) calculations within the generalized gradient approximation (GGA) using the Perdew-Burke-Ernzerhof (PBE) formulation. The projected augmented wave (PAW) potential [29,30] was chosen to describe the ionic cores and take valence electrons into account using a plane wave basis set with a kinetic energy cutoff of 400 eV. Partial occupancies of the Kohn-Sham orbitals were allowed using the Gaussian smearing method and a width of 0.05 eV. The electronic energy was considered self-consistent when the energy change was smaller than 10^{-5} eV. A geometry optimization was considered convergent when the force change was smaller than 0.02 eV/Å. Grimme's DFT-D3 methodology [31,32] was used to describe the dispersion interactions.

First, we constructed the monomer form of $AlCl_3$ molecule and calculated the energy of the molecule. According to EDS characterizations, SiO_2 shows the highest proportion in the ternary metal oxides. Therefore, SiO_2 was considered as the substrate, Al atoms and the third kinds of metal atom were doped into different structural models according to observed chemical compositions. Applying this principle, hexagonal SiO_2 cells were constructed, and the optimized lattice constants are of $a = 4.764$ Å and $c = 5.317$ Å. Based on the optimized lattice constants, we defined the SiO_2 (001) surface using 24 Si and 48 O atoms. The eight dangling O atoms exposing to both sides are normally saturated with H atoms (see Fig. S3). Subsequently, four different support models were constructed by modifying the top layer of the model with Al and Me atoms (Me = Mg, La, Ni or Ga), and the structure models are illustrated in Fig. 1.

The interaction energy (E_{in}) between the supports and the active components of $AlCl_3$ or Al_2Cl_6 can be calculated using Equation (2):

$$E_{in} = -\left(E_{cat} - \left(E_{sup} + E_{act}\right)\right) \tag{2}$$

where E_{cat}, E_{sup} and E_{act}, represent the energies of the catalyst, support and active species of $AlCl_3$ or Al_2Cl_6 in a cubic periodic box with a side length of 20 Å and a 1 × 1 × 1 Monkhorst-Pack k-point grid for Brillouin zone sampling.

3. Results and discussion

3.1. Characterizations of supports and catalysts

3.1.1. Pore structure characterization

The pore structures of supports can largely determine the immobilization of active components and thus lead to distinct catalytic performances [33]. The pore characteristics are shown in Table 1 as determined from the N_2 adsorption of four ternary composite supports containing different metal oxides. It can be seen that the S-3 support has the largest specific surface area of 170.58 m^2/g and the smallest average pore size of 9.32 nm. Previous studies have demonstrated that the Si to Al molar ratio, n (Si)/n (Al), had a remarkable impact on the surface area of support, which can affect the loading amounts of active components as well as the catalytic efficiency [26]. Further experiments indicate that S-3 support (with n (Si)/n (Al) of 9.76, see Table S2) can load the largest amount of active components. Based on the chemical composition of S-3, three supports of S-3-1, S-3-2 and S-3-3 were thereby prepared by changing the Si/Al ratio (respectively with n (Si)/n (Al) of 4.86, 6.61, 12.30, see Table S2). Their characterization results are shown in Table 2. From the pore size distribution of the different supports, as shown in Fig. 2, both the chemical composition and n (Si)/n (Al) show slight effects on the pore size distribution of the supports (ranging from 80 to 110 nm).

3.1.2. TG analysis

In order to understand the combining form of $AlCl_3$ species with the different supports, supported catalysts were subjected to TG analysis in an oxygen atmosphere (See Fig. 3). All TG curves can be divided into two regions: the first region with temperature ranging from RT to 300 °C and the second one ranging from 420 to 600 °C. The first weight loss event is responsible for the sublimation of free $AlCl_3$ [34]. As for this event, M − 2 and M − 4 show larger DTG peaks than M − 1 and M-3. The second mass loss event can be attributed to the unloading of the guest species from the supports. Due to the host-guest interactions between the supports and active species, the anchored $AlCl_3$ species need to be desorbed at a higher treatment temperature. The results clearly demonstrate that M − 3 sample gives the largest DTG peak in the high temperature region centered at 522 °C, and the M − 3 support hosts more active components which may result from stronger host-guest interactions.

3.1.3. XPS characterization

In order to reveal the Al species in the supports, XPS characterization was performed on the fresh and spent catalysts [35–37]. XPS spectra for the fresh catalyst samples show the Al $2p_{1/2}$ peak located at around 75.5 eV (see Fig. 4(a–d)), which is 1.1 eV higher than the binding energy of Al

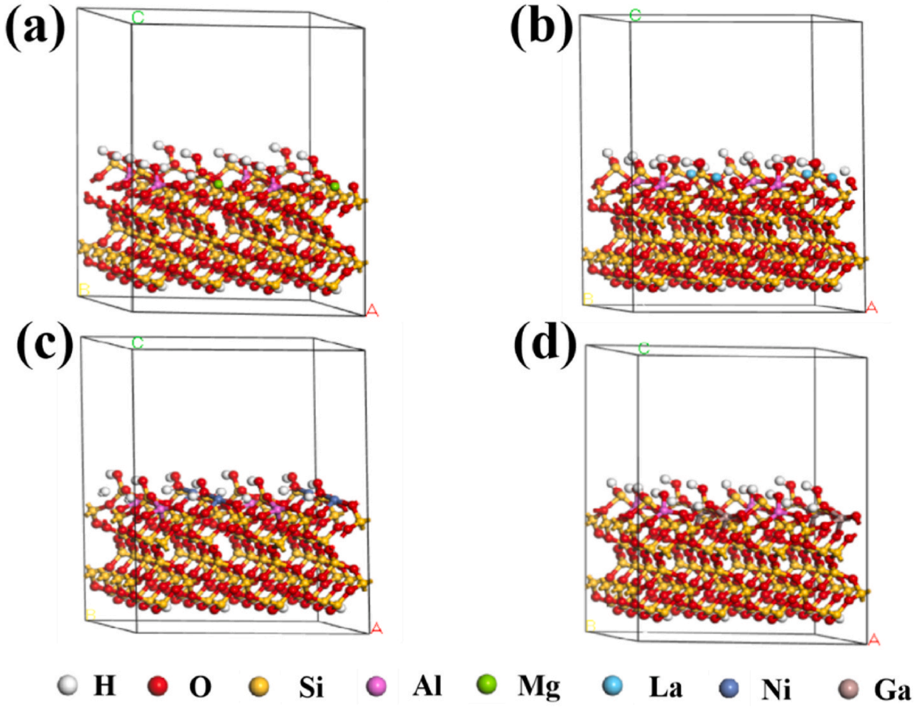

Fig. 1. Structure models for different supports (a: S-1, b: S-2, c: S-3, d: S-4).

Table 1
Pore structure characterizations of the different supports.

Support	S_{BET}[a] (m^2/g)	V_p[b] (cm^3/g)	d_p[c] (nm)
S-1	140.12	0.36	10.41
S-2	154.47	0.40	10.20
S-3	170.58	0.40	9.32
S-4	128.89	0.36	11.11

[a] Specific surface area.
[b] Pore volume.
[c] Average pore diameter (1.7–300 nm).

Table 2
Effects of n (Si)/n (Al) on pore structures of supports.

Support	S_{BET} (m^2/g)	V_p (cm^3/g)	d_p (nm)
S-3-1	162.42	0.37	9.49
S-3-2	157.09	0.34	9.76
S-3	170.58	0.40	9.32
S-3-3	154.69	0.36	10.32

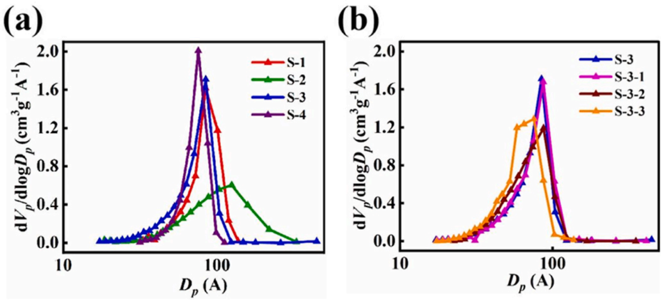

Fig. 2. Pore size distributions of the different supports.

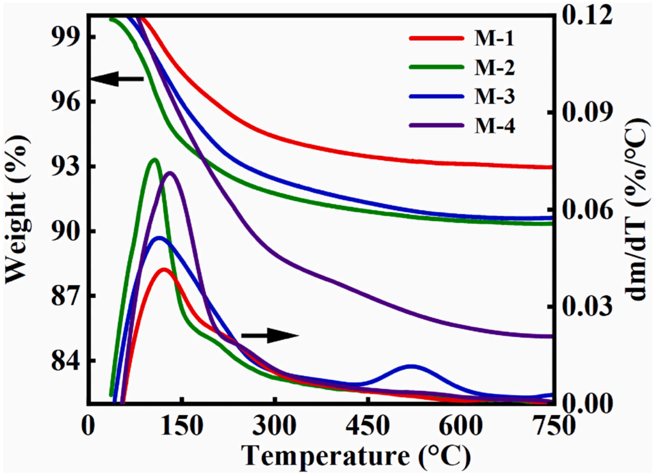

Fig. 3. TG-DTG curves for different catalysts.

$2p_{1/2}$ in bulk $AlCl_3$. The increase in binding energy is mainly due to the substitution of Cl in $AlCl_3$ by O-containing groups of the support. In Fig. 4(e), the binding energy of Al species Al $2p_{1/2}$ involved in the used catalyst is 74.85 eV, which is about 0.65 ev lower than that of the fresh catalyst. The XPS peak strength for the used catalyst is significantly weaker than that of the fresh sample (see Fig. 4(f)), indicating the loss of the active component during the oligomerization reaction. Previous investigations [26] suggested that the active component could be bonded with the hydroxyl group on the support surfaces, and Al mainly existed in three forms, i.e. Al_2O_3–O–$AlCl_2$, (Al_2O_3–O)$_2$–AlCl and free $AlCl_3$, respectively. Among them, Al_2O_3–O–$AlCl_2$ is considered to be the main structure that shows catalytic activity. In section 3.6, the specific bonding mode between $AlCl_3$ and the support surface will be calculated by constructing the molecular model based on experimental characterization results.

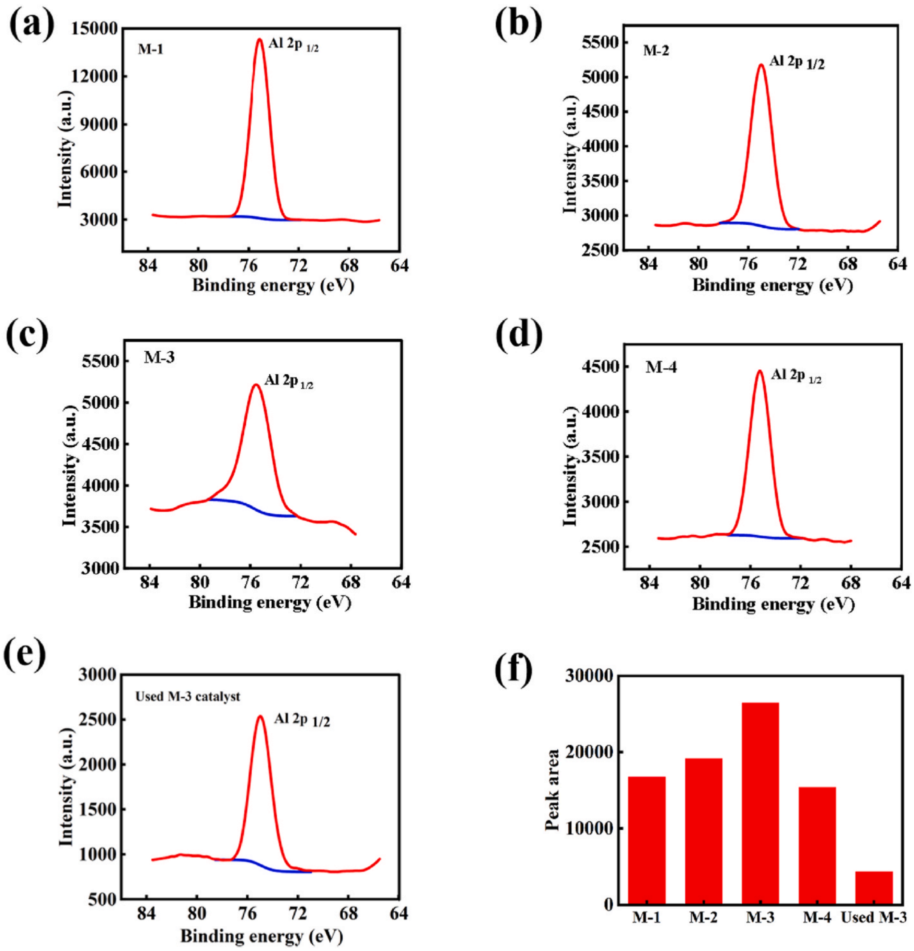

Fig. 4. Al XPS spectra and peak areas of fresh and spent catalysts. (Al XPS spectra of (a) fresh M − 1, (b) fresh M − 2, (c) fresh M − 3, (d) fresh M − 4, and (e) used M − 3, (f) XPS peak areas of different catalysts).

3.1.4. *Py-IR characterization*

The acidity of different catalysts was measured using the Py-IR characterization and the results are presented in Fig. 5. All catalysts show a strong absorption peak at 1445 cm^{-1}, corresponding to the adsorption on Lewis acid sites. According to integration of peak areas of two supported catalysts, the M − 3 sample has a larger absorption peak (8.21%·cm^{-1}) compared to the M − 1 (2.40%·cm^{-1}), indicating that the M − 3 catalyst has more Lewis acid sites and therefore exhibits higher catalytic activity [38,39]. A weak absorption peak at 1540 cm^{-1} can be assigned to the interaction between the pyridine molecule and the Brønst acid. In addition, all catalysts exhibited a strong peak at 1490 cm^{-1} that is caused by the combined action of Brønst acid and Lewis acid.

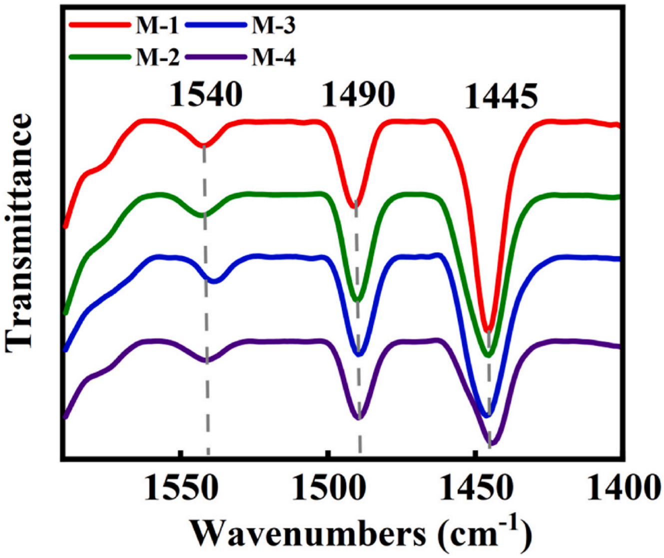

Fig. 5. Py-IR spectra of the different catalysts.

3.2. *Effects of compositions of supports*

The catalytic activity and stability of the supported catalysts are two of the most important performances of catalysts, a promising catalyst should have both high activity and excellent stability. First, catalytic oligomerization experiment was carried out in a batch reactor to examine the activity of the catalysts. As shown in Fig. 6, it can be found that the maximum chlorine content of M − 3 catalyst is 22.0%, and the yield of the oligomerized product is 98.09%. The employment of M − 1, reported in our previous work as well, gave rise to lower chlorine content and yield than that of M − 2 and M-3. While the presence of M − 4 catalyst results in the lowest chlorine content of 14.25% and the lowest product yield of 72.82%. Fig. 7 shows the relationship among the specific surface areas of the supports, the chlorine contents of the catalysts, and the yields of products. The specific surface areas of M − 1, M − 2, M − 3, M − 4 were 140.12, 154.47, 170.58, and 128.89 m^2/g, respectively. As the specific surface areas of these supports with different chemical compositions increases, both the chlorine content and product yield show increasing trend. The chemical compositions of ternary oxide

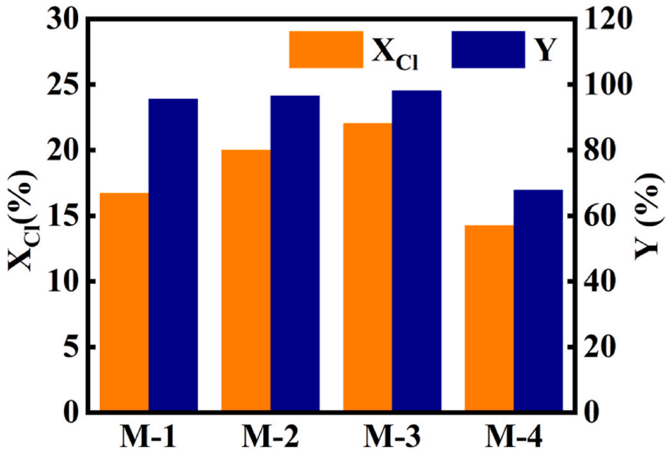

Fig. 6. Chlorine contents (X_{Cl}) and PAO yields (Y) in cases of catalysts prepared using different supports.

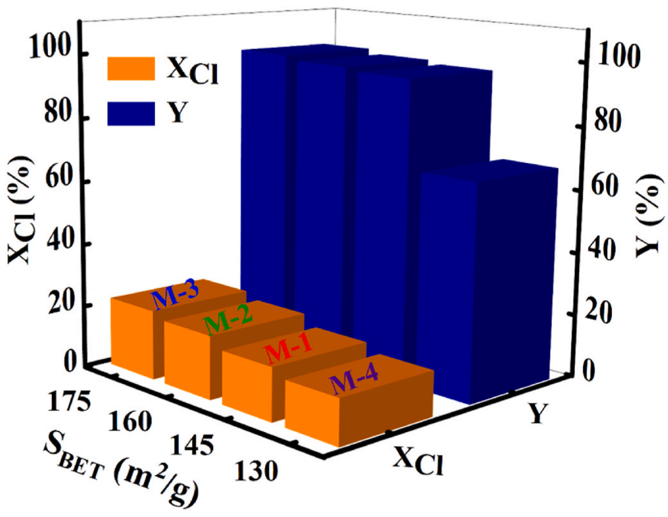

Fig. 7. The relationship among the specific surface area of the support, chlorine contents (X_{Cl}) and PAO yields (Y).

supports and the derived catalysts are listed in Tables S1 and S2. Four different supports have distinct chemical compositions along with the variations of their structures, which is responsible for the evolution of the specific surface areas. As the number of active sites that can be loaded increases with the specific surface areas, therefore giving rise to increasing loading capacity.

A custom-made fixed-bed reactor was then used to assess the stability of all catalysts, and the effects of various factors on stability of catalyst were investigated (see Fig. 8). After 3 h of reaction, the product yield ranks in the following sequence: M − 3 > M − 2 > M − 1 > M-4. However, the yield decreases significantly with increasing reaction time. After 27 h, the reaction in the presence of M − 3 catalyst gives a product yield of 71.34%. According to the yields obtained at reaction times of 3 h and 27 h, catalysts M − 1, M − 2, M − 3 and M − 4 exhibit the activity loss of 32.52%, 31.46%, 26.75% and 36.00%, respectively, undergoing interval 24-h of reaction time. These results demonstrate that M − 3 catalysts are more stable and have a slower loss rate of the active components than other catalysts. In the case of M − 4 catalyst sample, the product yield is reduced from 72.82% to 36.82% after a 24-h reaction, indicating the lowest stability. Theoretical calculations will be used to identify the mechanism for structure determining the stability. In Table S3, all PAO products synthesized with different supported catalysts show comparative viscosity as well as freezing point.

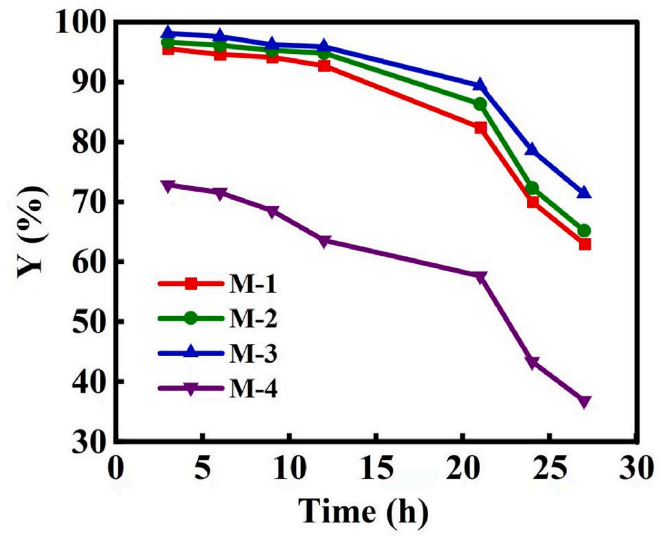

Fig. 8. PAO yield (Y) obtained from the reactions in cases of catalysts prepared using different supports.

3.3. Effects of n(Si)/n(Al) of supports

Fig. 9 shows that all catalysts with different n (Si)/n (Al) have high catalytic activity. Among them, the M − 3 catalyst exhibits the highest initial Y of 98.09% and the highest X_{Cl} of 22.0%, while the M-3-3 catalyst has the lowest initial Y of 90.57% and the lowest X_{Cl} of 17.34%. The combined results are shown in Table 2, the differences in stability can be found to be mainly related to the loading of the active components and the pore structures of the supports, which is consistent with the increase in X_{Cl} of the catalyst and Y with increasing specific surface area. Fig. 10 shows the variation of Y with time for the supported catalysts with different n (Si)/n (Al). All catalysts with an initial Y of above 90% exhibits varying degrees of deactivation with increasing reaction time. Among them, after a continuous reaction for 27 h with M − 3 catalyst, the yield of product could still maintain 71.34%, suggesting the best stability of M − 3 catalyst. While for the case of M-3-3, the yield of product drops to 45.23%, indicating its worst stability. Compared with M − 3 catalyst, M-3-1 and M-3-2 catalysts also show lower stability. The properties of PAO synthesized in the presence of supported catalysts prepared with different n (Si)/n (Al) are shown in Table S4.

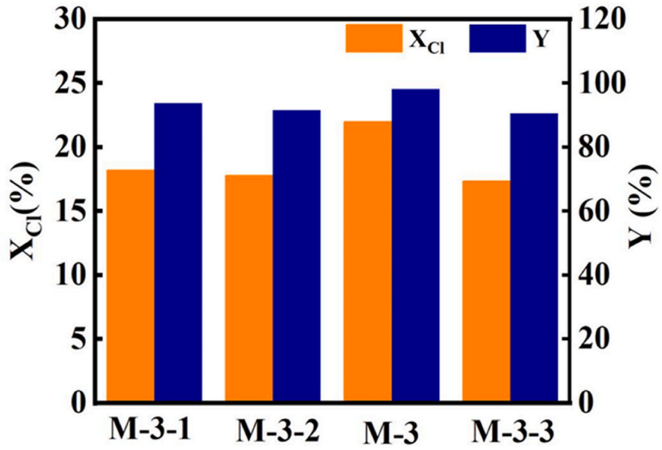

Fig. 9. Chlorine contents (X_{Cl}) and PAO yields (Y) in cases of catalysts prepared using different n (Si)/n (Al).

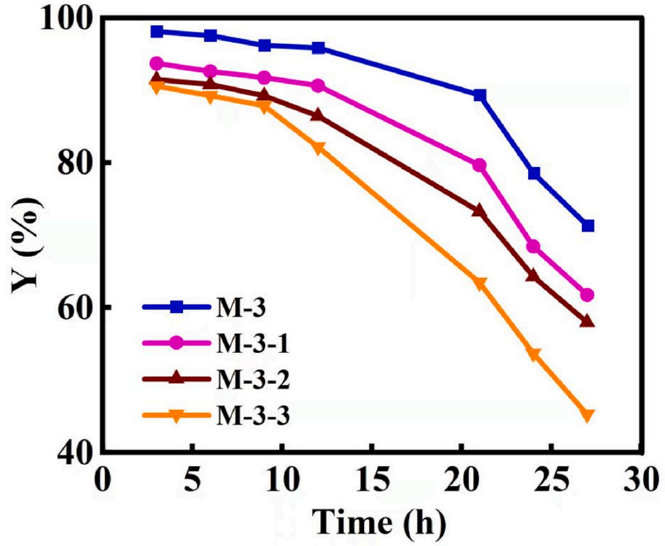

Fig. 10. PAO yields (Y) in cases of catalysts prepared using different *n* (Si)/ *n* (Al).

3.4. *Effects of active component loading*

In order to obtain the optimum loading of active components, the activity of the supported catalysts and the properties of the oligomerization products were determined by adjusting the mass ratio of active component to support. The results clearly show that the initial mass ratio of active component to support has a significant effect on the chlorine content of the catalyst. As shown in Fig. 11, when the mass ratio of active component to support increased from 0.3 for M-3-4 to 0.5 for M-3-5, the chlorine content of the catalyst increases from 17.90% to 22.48% while the yield of PAO increases from 96.87% to 98.17%. This indicates that the more active components there are, the higher the yield of the corresponding oligomers can be obtained. The viscosity of the resulting PAO increases with increasing active component loading, suggesting that the high active component content promotes 1-decene conversion to oligomers with high molecular weight. Fig. 12 shows the activity of the supported catalysts prepared with different active component loads as a function of time. The activity evolution of M − 3 is basically similar to that of M-3-5. After 27 h, the final oligomerization yields in the case of M − 3 and M-3-5 could be maintained at around 70%. While the deactivation rate of sample M-3-4 with the least active components is the fastest. From previous studies [26], the loss of active component contributes to catalyst deactivation largely. With the increase of reaction time, M-3-4 catalyst with lower active component load has the faster activity decay. Also, all synthesized PAO products show similar properties. In the consideration of economic usage of active component, the M − 3 sample was selected as the optimal catalyst for the following studies.

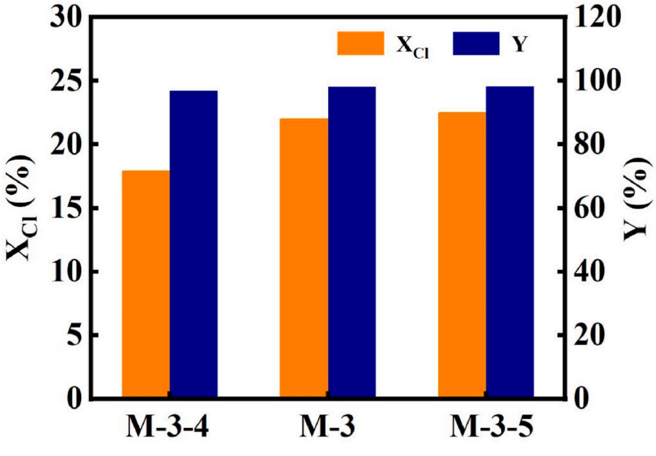

Fig. 11. Chlorine contents (X_{Cl}) and PAO yields (Y) in cases of catalysts prepared using different loading of active components.

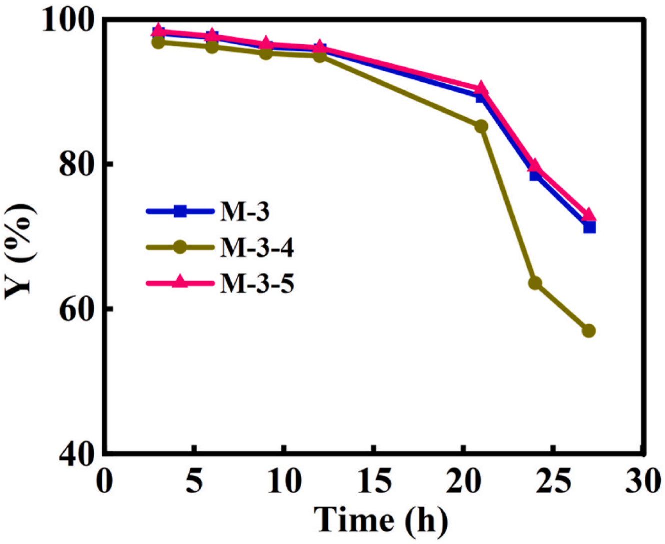

Fig. 12. PAO yield (Y) in cases of catalysts prepared using different loading of active components.

3.5. *Deactivation mechanism of the support catalysts during 1-decene oligomerization*

In order to further insight into the loading of active components on the supports and deactivation mechanism, scanning electron microscopy (SEM) was used to characterize the surface morphology of the M − 3 catalyst. For the fresh M − 3 catalyst, rich pore structures on the catalyst surface are clearly observed at a magnification of 2 × 10^4 times (See Fig. 13(a)). At a magnification of 5 × 10^4 times (see inset in the top right-hand corner of Fig. 13(a)), the micro-pore channels of the catalyst are clearly observed and the active components are well dispersed on the surface of the support [40,41]. In Fig. 13(b), it is apparent that the porous structures of the catalysts has almost completely disappeared after undergoing oligomerization reaction [42].

To further understand the loss of active components on the supports, TEM characterizations were performed on the supports, fresh and deactivated catalysts. As shown in Fig. 13(c), the composite oxide support is composed of uniformly dispersed nanoparticles with a size of 15–30 nm, indicating the uniform distributions of ternary oxides in support [43]. As observed from Fig. 13(d), the surface of catalyst is full of sponge-like substances, which implies that the active components are well distributed on the ternary oxide composite support [44,45]. After the oligomerization reaction, the deactivated catalyst was characterized as well (see Fig. 13(e)). It is found that the spongy substances gradually disappear with the aggregating of the nanoparticles, indicating the loss of the active components. These results suggest that the deactivation of the catalyst is due to the loss of the active components.

As the effect of oligomerization products on the pore structure of the catalyst is another important factor that leads to the deactivation of the supported catalyst, the pore structures of the fresh and deactivated M − 3 catalyst were analyzed, respectively. As shown in Table 3, after loading the active components, the specific surface area and pore volume of the support decrease, while the average pore diameter increase (the BET analysis results of the support are shown in Table 1). The results show that the grafted active components preferentially occupy

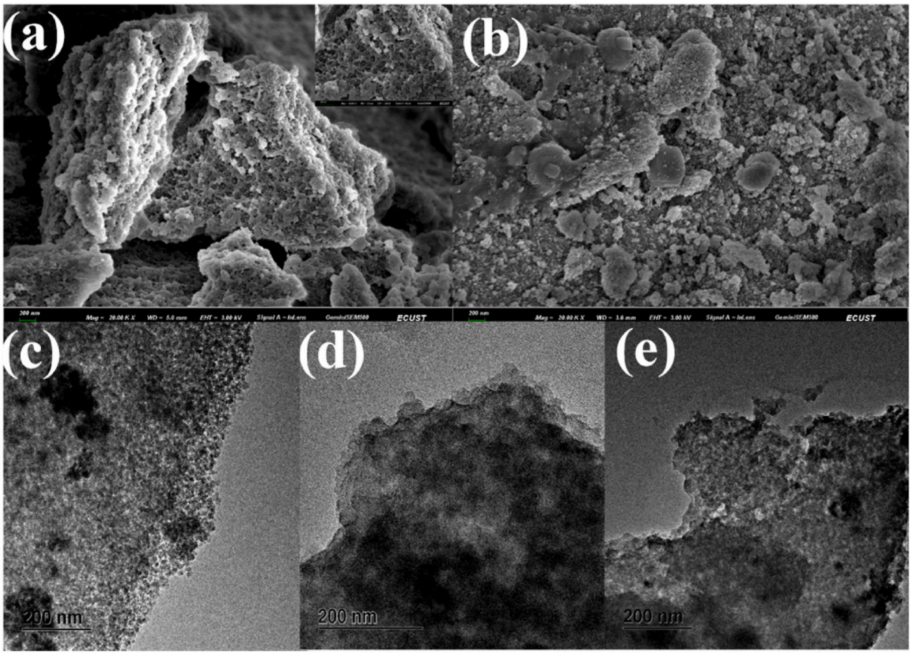

Fig. 13. SEM images of (a) fresh, (b) used M − 3 catalyst and TEM images of (c) S-3 support, (d) fresh, (e) used M − 3 catalysts.

Table 3
BET specific surface area, pore volume, average pore diameter and chlorine content of fresh and used M − 3 catalysts.

Sample	Pore structure			X_{Cl} (%)
	S_{BET} (m^2g^{-1})	V_p ($cm^3\ g^{-1}$)	d_p (nm)	
Fresh	46.84	0.103	10.05	22.00
Used	48.87	0.094	9.81	17.89

small pores. After 28 h of the reaction, the specific surface area of the M − 3 catalyst slightly increases from 46.84 to 48.87 m^2/g, and the average pore size decreases from 10.05 to 9.81 nm, which is probably ascribed to the recovery of the previously occupied small pore structures because of the loss of the active components. The chlorine content of the catalyst decreases from 22.00% to 17.89% which can also be explained by the loss of the active component. Characterizations by SEM, TEM and BET offer a more intuitive identification for the deterioration in catalyst performance [46,47].

3.6. DFT calculations

Furthermore, the binding energy between the active components and the support were calculated by using DFT to explain the loss of the active components [48,49]. According to the EDS and XPS analyses, the chemical compositions of four supports S-1, S-2, S-3 and S-4 can be defined as $(MgO)_{2.122}(Al_2O_3)$ $(SiO_2)_{19.516}$, $(La_2O_3)_{1.394}(Al_2O_3)$ $(SiO_2)_{19.516}$, $(NiO)_{2.168}(Al_2O_3)$ $(SiO_2)_{19.516}$, and $(Ga_2O_3)_{1.301}(Al_2O_3)$ $(SiO_2)_{19.516}$, respectively, based on one Al_2O_3. According to these determined chemical compositions, the support models were defined and their structures were optimized. For structural optimization, the gamma point in the Brillouin zone was used for *k*-point sampling, and the bottom stoichiometric layer was fixed while the top one was allowed to relax. Subsequently, the energy was calculated from the optimized support model. Active component $AlCl_3$ was adsorbed and immobilized on the surface of the support to obtain a catalyst model (see Fig. 14). Finally, the energy of each catalyst model was calculated [50,51].

As can be seen from Fig. 15, the active components on M − 2 catalyst combine with the oxygen on the surface of the support to form Al_2O_3-–O–$AlCl_2$, with a correspondingly higher binding energy. The distance between the active components on M − 1 as well as M − 4 catalysts and the oxygen exposing on the support is about 2.18 Å, which could to be considered to form a weak bond with small binding energy [52]. However, the active component on M − 3 catalyst not only forms weak bonds with the oxygen atoms exposing on the support, but also directly binds with the metallic nickel, which has a higher binding energy than the other three catalysts. These results are summarized in Fig. 16, which shows that the binding energy of the active component $AlCl_3$ following the sequence of M − 3 > M − 2 > M − 1 > M-4. Considering that $AlCl_3$ may exist as dimer, the dimer model of $AlCl_3$ was established and adsorbed onto the four constructed support models. The calculation results indicate that two Al atoms are completely surrounded by six Cl atoms, therefore are incapable of bonding to the surface atoms. The other six Cl atoms are also weak in bonding with the surface atoms; thus, the obtained binding energy is very small. As a result, it can be concluded that $AlCl_3$ is bound to the support in the form of monomer.

Based on the DFT calculations, the binding energy of the support and the active components can be obtained from molecular simulations to verify the experimental results. Therefore, the loaded amount and loss rate of the active components can be largely determined by the binding energy. To explain the difference in binding energy due to the different support composites, the average ionic potential of the support was calculated using Equation (3) [53]:

$$\varnothing = \frac{\sum X_i \left(\frac{Z}{r}\right)}{\sum X_i} \tag{3}$$

where X_i is mole fraction, Z is charge, and r is ionic radius. The relationship between binding energy and average ionic potential are shown in Fig. 17. For all catalyst samples, the energy released by the active components loaded on the support decreases with increase in the average ion potential of the corresponding support. Under the condition with the same electron configuration, higher average ionic potential of support results in higher polarization force, therefore more difficult binding of the active component with the support, and smaller binding energy.

These DFT calculation results suggest that it is essential to introduce metal atoms with a lower ionic potential into the supports for the development of a catalyst with higher activity and stability, owing to

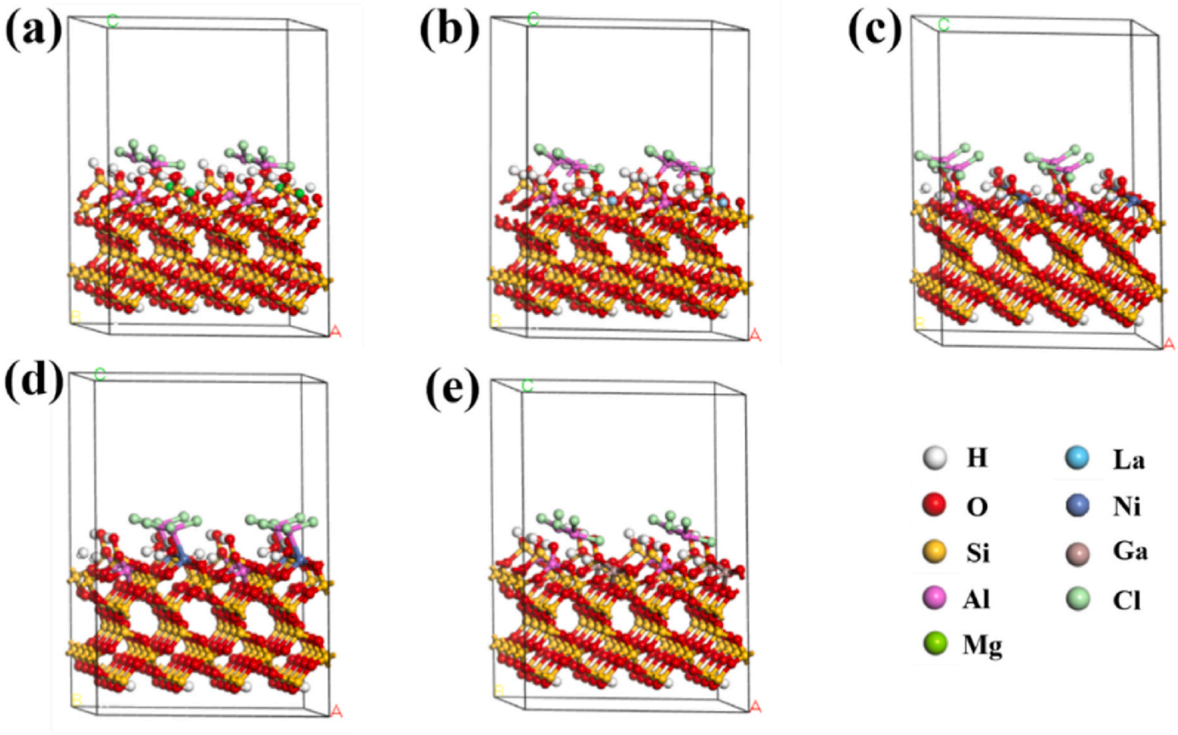

Fig. 14. Support surface and $AlCl_3$ binding model diagram (a: the oxygen atom on the surface of the S-1 support binds to Al, b: the oxygen atom on the surface of the S-2 support binds to Al, c: the oxygen atom on the surface of the S-3 support binds to Al, d: the nickel atom on the surface of the S-3 support combines with Al, e: the oxygen atom on the surface of the S-4 support binds to Al).

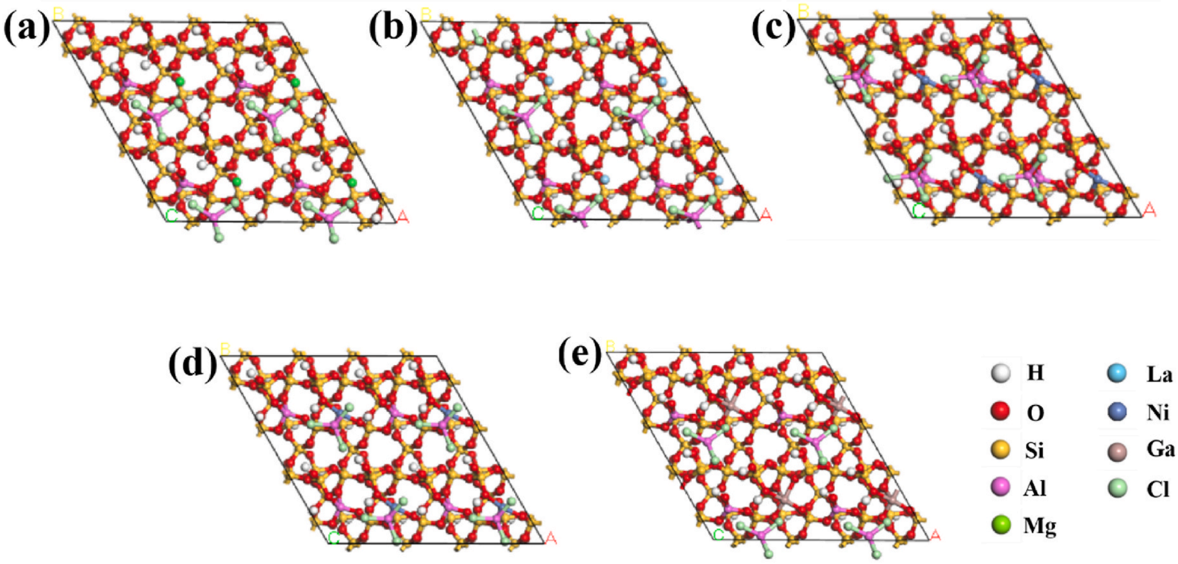

Fig. 15. Adsorption and binding of $AlCl_3$ on different supports (a: M − 1, b: M − 2, c, d: M − 3, e: M − 4).

stronger binding interaction between the active components and the metal oxide-derived supports.

4. Conclusions

By introducing different metal oxides, we have obtained a series of supported catalysts by impregnating $AlCl_3$ on resynthesized ternary metal oxide supports, i.e., La_2O_3–Al_2O_3–SiO_2, NiO–Al_2O_3–SiO_2 and Ga_2O_3–Al_2O_3–SiO_2. Our investigations demonstrate that the catalyst supported by NiO–Al_2O_3–SiO_2 shows the highest activity and stability. BET characterizations show that the catalyst with higher load has a larger specific surface area, which provides more sites for hosting the active components. In addition, the activity and stability of the catalyst are well explained by DFT calculations. We have found that the host-guest interaction energy increases with decreasing average ionic potential of ternary oxide composites. Furthermore, the calculations indicate that the M − 3 catalyst shows the highest stability owing to the largest binding energy, which is unanimous with the conclusion drawn from the experiments.

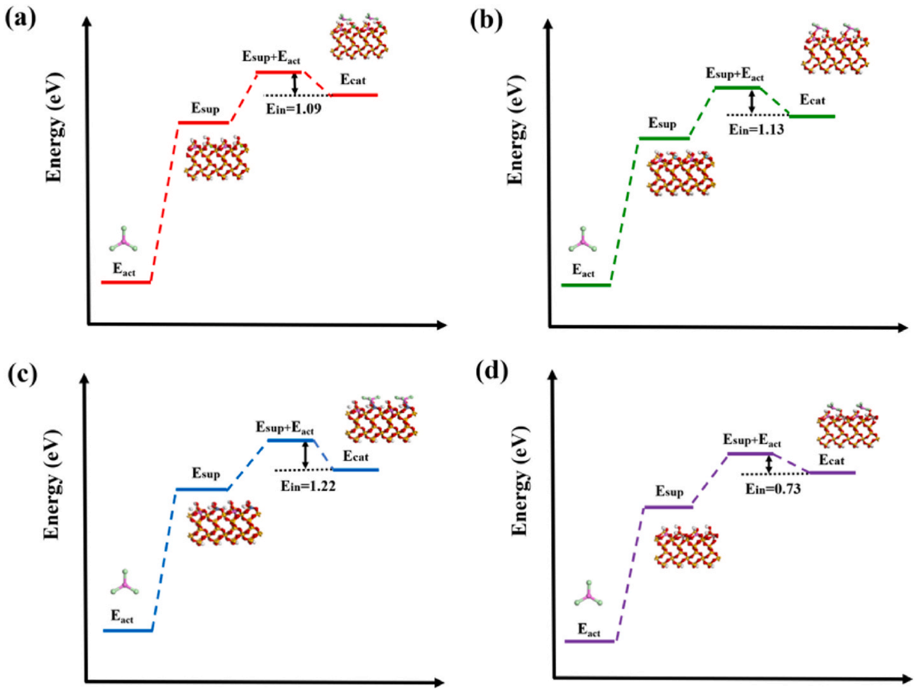

Fig. 16. Calculated results of binding energy of the $AlCl_3$ onto different supports (a: M − 1, b: M − 2, c: M − 3, d: M − 4).

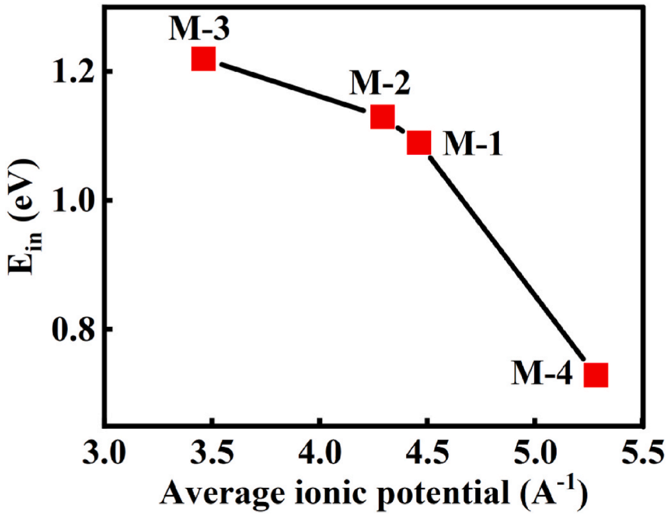

Fig. 17. Relationship between binding energy and the average ionic potential of the support.

CRediT authorship contribution statement

Yue Lou: Resources, Investigation, Writing – original draft. **Yuxiang Chen:** Investigation, Writing – original draft. **Yang Zhao:** Methodology. **Cheng Qian:** Data curation. **Cheng Niu:** Data curation. **Hao Jiang:** Formal analysis. **Chuanlei Liu:** Investigation. **Kongguo Wu:** Validation. **Benxian Shen:** Conceptualization. **Jian Long:** Methodology, Supervision. **Yiming Wang:** Validation, Writing – review & editing, Supervision. **Hui Sun:** Conceptualization, Investigation, Writing – review & editing, Supervision. **Jigang Zhao:** Resources. **Jichang Liu:** Methodology. **Hao Ling:** Validation. **Di Wu:** Conceptualization. **Yujun Tong:** Methodology.

Declaration of competing interest

The authors declare that they have no known competing financial interests or personal relationships that could have appeared to influence the work reported in this paper.

Acknowledgments

This work is financially supported by the National Natural Science Foundation of China (Grant 21878097 and 22178109) and the Natural Science Foundation of Shanghai (Grant 21ZR1417700). D.W. acknowledges the institutional funds from the Gene and Linda Voiland School of Chemical Engineering and Bioengineering, and the Alexandra Navrotsky Institute for Experimental Thermodynamics at Washington State University.

Appendix A. Supplementary data

Supplementary data to this article can be found online at https://doi.org/10.1016/j.micromeso.2021.111665.

References

[1] G.D. Yadav, N.S. Doshi, Development of a green process for poly-α-olefin based lubricants, Green Chem. 4 (2002) 528–540, https://doi.org/10.1039/B206081G.

[2] S. Boyde, Green lubricants. Environmental benefits and impacts of lubrication, Green Chem. 4 (2002) 293–307, https://doi.org/10.1039/B202272A.

[3] A. Finiels, F. Fajula, V. Hulea, Nickel-based solid catalysts for ethylene oligomerization – a review, Catal. Sci. Technol. 4 (2014) 2412–2426, https://doi.org/10.1039/C4CY00305E.

[4] Y.P. Li, Z.Q. Li, B. Zhou, M.L. Li, X.S. Xue, S.F. Zhu, Q.L. Zhou, Chiral spiro phosphoric acid-catalyzed friedel–crafts conjugate addition/enantioselective protonation reactions, ACS Catal. 9 (2019) 6522–6529, https://doi.org/10.1021/acscatal.9b01502.

[5] B. Xiang, T.F. Xu, L. Wu, R.R. Liu, J.R. Gao, Y.X. Jia, Lewis acid catalyzed friedel–crafts alkylation of alkenes with trifluoropyruvates, J. Org. Chem. 81 (2016) 3929–3935, https://doi.org/10.1021/acs.joc.6b00358.

[6] J. Sun, Y. Gui, Y. Huang, J. Li, Z. Zha, Y. Yang, Z. Wang, Lewis acid-catalyzed enantioselective friedel–crafts alkylation of pyrrole in water, ACS Omega 5 (2020) 11962–11970, https://doi.org/10.1021/acsomega.9b04115.

[7] S.N. Kessler, H.A. Wegner, Lewis acid catalyzed inverse electron-demand Diels−Alder reaction of 1,2-diazines, Org. Lett. 12 (2010) 4062–4065, https://doi.org/10.1021/ol101701z.

[8] X.S. Zhao, M.G.Q. Lu, C. Song, Immobilization of aluminum chloride on MCM-41 as a new catalyst system for liquid-phase isopropylation of naphthalene, J. Mol. Catal. 191 (2003) 67–74, https://doi.org/10.1016/S1381-1169(02)00366-7.

[9] S. Constant, C. Basset, C. Dumas, F. Di Renzo, M. Robit zer, A. Barakat, F. Quignard, Reactive organosolv lignin extraction from wheat straw: influence of Lewis acid catalysts on structural and chemical properties of lignins, Ind. Crop. Prod. 65 (2015) 180–189, https://doi.org/10.1016/j.indcrop.2014.12.009.

[10] A.P. Wight, M.E. Davis, Design and preparation of Organic−Inorganic hybrid catalysts, Chem. Rev. 102 (2002) 3589–3614, https://doi.org/10.1021/cr010334m.

[11] C. del Pozo, A. Corma, M. Iglesias, F. Sánchez, Immobilization of (NHC)NN-pincer complexes on mesoporous MCM-41 support, Organometallics 29 (2010) 4491–4498, https://doi.org/10.1021/om1006352.

[12] A. Kermagoret, R.N. Kerber, M.P. Conley, E. Callens, P. Florian, D. Massiot, F. Delbecq, X. Rozanska, C. Copéret, P. Sautet, Chlorodiethylaluminum supported on silica: a dinuclear aluminum surface species with bridging μ2-Cl-ligand as a highly efficient co-catalyst for the Ni-catalyzed dimerization of ethene, J. Catal. 313 (2014) 46–54, https://doi.org/10.1016/j.jcat.2014.02.006.

[13] R. Deng, K. You, L. Yi, F. Zhao, J. Jian, Z. Chen, P. Liu, Q. Ai, H.a. Luo, Solvent-free, low-temperature, highly efficient catalytic nitration of toluene with NO_2 promoted by molecular oxygen over immobilized $AlCl_3$–SiO_2, Ind. Eng. Chem. Res. 57 (2018) 12993–13000, https://doi.org/10.1021/acs.iecr.8b02786.

[14] K. Hernadi, E. Couteau, J.W. Seo, L. Forró, O.H. Al(, $_3$/Multiwalled carbon nanotube composite:homogeneous coverage of Al (OH)3_on carbon nanotube surfaces, Langmuir 19 (2003) 7026–7029.

[15] K. Wen, J. Zhu, H. Chen, L. Ma, H. Liu, R. Zhu, Y. Xi, H. He, Arrangement models of keggin-Al_{30} and keggin-Al_{13} in the interlayer of montmorillonite and the impacts of pillaring on surface acidity: a comparative study on catalytic oxidation of toluene, Langmuir 35 (2019) 382–390, https://doi.org/10.1021/acs.langmuir.8b03447.

[16] J.M. Escola, R. Van Grieken, J. Moreno, R. Rodríguez, Liquid-Phase oligomerization of 1-hexene using Al-MTS catalysts, Ind. Eng. Chem. Res. 45 (2006) 7409–7414, https://doi.org/10.1021/ie0603262.

[17] S. Jiao, H. Lei, J. Tu, J. Zhu, J. Wang, X. Mao, An industrialized prototype of the rechargeable Al/AlCl3-[EMIm]Cl/graphite battery and recycling of the graphitic cathode into graphene, Carbon 109 (2016) 276–281, https://doi.org/10.1016/j.carbon.2016.08.027.

[18] K.P. Borujeni, B. Tamami, Polystyrene and silica gel supported $AlCl_3$ as highly chemoselective heterogeneous Lewis acid catalysts for Friedel–Crafts sulfonylation of aromatic compounds, Catal. Commun. 8 (2007) 1191–1196, https://doi.org/10.1016/j.catcom.2006.10.028.

[19] M. Gu, Z. Cheng, Carboxylation of toluene with CO_2 over dimeric $AlCl_3$ immobilized on alumina, Ind. Eng. Chem. Res. 53 (2014) 9992–9998, https://doi.org/10.1021/ie5004762.

[20] S. Karimi, S. Sadjadi, N. Bahri-Laleh, M. Nekoomanesh-Haghighi, New less-toxic halloysite-supported ionic liquid/$AlCl_3$ oligomerization catalysts: a comparative study on the effects of various ionic liquids on the properties of polyalphaolefins, Mol. Catal. 509 (2021) 111648, https://doi.org/10.1016/j.mcat.2021.111648.

[21] M. Mashayekhi, S. Talebi, S. Sadjadi, N. Bahri-Laleh, Production of polyalfaolefin-based lubricants using new (poly)ionic liquid/$AlCl_3$ catalysts as environmentally friendly alternatives to commercial $AlCl_3$ route, Appl. Catal. Gen. 623 (2021) 118274, https://doi.org/10.1016/j.apcata.2021.118274.

[22] M. Tabrizi, N. Bahri-Laleh, S. Sadjadi, M. Nekoomanesh-Haghighi, The effect of ionic liquid containing $AlCl_3$ catalytic systems on the microstructure and properties of polyalphaolefin based lubricants, J. Mol. Liq. 335 (2021) 116299, https://doi.org/10.1016/j.molliq.2021.116299.

[23] Y. Peng, M. Dong, X. Meng, B. Zong, J. Zhang, Light FCC gasoline olefin oligomerization over a magnetic $NiSO_4$/γ-Al_2O_3catalyst in a magnetically stabilized bed, AIChE J. 55 (2009) 717–725, https://doi.org/10.1002/aic.11712.

[24] Q. Huang, L. Chen, Y. Sheng, L. Ma, Z. Fu, W. Yang, Synthesis and characterization of oligomer from 1-decene catalyzed by $AlCl_3/TiCl_4/SiO_2/Et_2AlCl$, J. Appl. Polym. Sci. 101 (1) (2006) 584–590, https://doi.org/10.1002/app.23530, 2006, 101, 584-590.

[25] H. Sun, B. Shen, D. Wu, X. Guo, D. Li, Supported Al–Ti bimetallic catalysts for 1-decene oligomerization: activity, stability and deactivation mechanism, J. Catal. 339 (2016) 84–92, https://doi.org/10.1016/j.jcat.2016.03.023.

[26] H. Sun, X. Lei, J. Tan, Z. Sun, X. Han, J. Liu, J. Zhao, B. Shen, X. Zhang, X. Guo, D. Wu, Tuning the catalytic activity and stability of Al–Ti bimetallic species immobilized on MgO–Al_2O_3–SiO_2 for 1-decene oligomerization, Ind. Eng. Chem. Res. 57 (2018) 6664–6672, https://doi.org/10.1021/acs.iecr.8b00791.

[27] G. Kresse, J. Furthmüller, Efficiency of ab-initio total energy calculations for metals and semiconductors using a plane-wave basis set, Comput. Mater. Sci. 6 (1996) 15–50, https://doi.org/10.1016/0927-0256(96)00008-0.

[28] G. Kresse, J. Furthmüller, Efficient iterative schemes for ab initio total-energy calculations using a plane-wave basis set, Phy. Rev. B. Condensed matter 54 (1996) 11169–11186, https://doi.org/10.1103/physrevb.54.11169.

[29] G. Kresse, D. Joubert, From ultrasoft pseudopotentials to the projector augmented-wave method, Phys. Rev. B. 59 (1999) 1758–1775, https://doi.org/10.1103/PhysRevB.59.1758.

[30] P.E. Blöchl, Projector augmented-wave method, Phy. Rev. B. Condensed matter 50 (1994) 17953–17979, https://doi.org/10.1103/PhysRevB.50.17953.

[31] Z. Tabandeh, A. Reisi-Vanani, Investigation of the adsorption behavior of two anticancer drugs on the pristine and BN-doped graphdiyne nanosheet: a DFT-D3 perception, Diam. Relat. Mater. 119 (2021) 108564, https://doi.org/10.1016/j.diamond.2021.108564.

[32] M.H. Darvishnejad, A. Reisi-Vanani, DFT-D3 calculations of the charge-modulated CO_2 capture of N/Sc-embedded graphyne: compilation of some factors, J. CO_2 Util. 46 (2021) 101469, https://doi.org/10.1016/j.jcou.2021.101469.

[33] Z. Wang, B. Gao, Preparation, structure, and catalytic activity of aluminum chloride immobilized on cross-linked polyvinyl alcohol microspheres, J. Mol. Catal. Chem. 330 (2010) 35–40, https://doi.org/10.1016/j.molcata.2010.06.028.

[34] S.K. Meher, G.R. Rao, Polymer-assisted hydrothermal synthesis of highly reducible shuttle-shaped CeO_2: microstructural effect on promoting Pt/C for methanol electrooxidation, ACS Catal. 2 (2012) 2795–2809, https://doi.org/10.1021/cs300473e.

[35] R. Grissa, A. Abramova, S.J. Tambio, M. Lecuyer, M. Deschamps, V. Fernandez, J. M. Greneche, D. Guyomard, B. Lestriez, P. Moreau, Thermomechanical polymer binder reactivity with positive active materials for Li metal polymer and Li-ion batteries: an XPS and XPS imaging study, ACS Appl. Mater. Interfaces 11 (2019) 18368–18376, https://doi.org/10.1021/acsami.9b01761.

[36] R. Grissa, V. Fernandez, N. Fairley, J. Hamon, N. Stephant, J. Rolland, R. Bouchet, M. Lecuyer, M. Deschamps, D. Guyomard, P. Moreau, XPS and SEM-EDX study of electrolyte nature effect on Li electrode in lithium metal batteries, ACS Appl. Energy Mater. 1 (2018) 5694–5702, https://doi.org/10.1021/acsaem.8b01256.

[37] M.A. Peck, M.A. Langell, Comparison of nanoscaled and bulk NiO structural and environmental characteristics by XRD, XAFS, and XPS, Chem. Mater. 24 (2012) 4483–4490, https://doi.org/10.1021/cm300739y.

[38] V. Krishna, G. Naresh, V.V. Kumar, R. Sarkari, A.H. Padmasri, A. Venugopal, Synthesis of 2,6-dimethylpyrazine by dehydrocyclization of aqueous glycerol and 1,2-propanediamine over CuCrO catalyst: rationalization of active sites by pyridine and formic acid adsorbed IR studies, Appl. Catal. B Environ. 193 (2016) 58–66, https://doi.org/10.1016/j.apcatb.2016.04.018.

[39] C.H. Zhou, G.L. Li, X.Y. Zhuang, P.P. Wang, D.S. Tong, H.M. Yang, C.X. Lin, L. Li, H. Zhang, S.F. Ji, W.H. Yu, Roles of texture and acidity of acid-activated sepiolite catalysts in gas-phase catalytic dehydration of glycerol to acrolein, Mol. Catal. 434 (2017) 219–231, https://doi.org/10.1016/j.mcat.2016.12.022.

[40] P.M. Csernica, J.R. McKone, C.R. Mulzer, W.R. Dichtel, H.D. Abruña, F.J. DiSalvo, Electrochemical hydrogen evolution at ordered Mo7Ni7, ACS Catal. 7 (2017) 3375–3383, https://doi.org/10.1021/acscatal.7b00344.

[41] M.-M. Millet, A.V. Tarasov, F. Girgsdies, G. Algara-Siller, R. Schlögl, E. Frei, Highly dispersed $Ni^0/Ni_xMg_{1-x}O$ catalysts derived from solid solutions: how metal and support control the CO_2 hydrogenation, ACS Catal. 9 (2019) 8534–8546, https://doi.org/10.1021/acscatal.9b02332.

[42] Q.T. Easter, V. Trauschke, S.A. Blum, Catalyst inefficiencies: supported ring-opening metathesis polymerization catalyst yields its ensemble rate from a small number of molecular active sites, ACS Catal. 5 (2015) 2290–2295, https://doi.org/10.1021/acscatal.5b00046.

[43] L. Xu, H. Song, L. Chou, One-pot synthesis of ordered mesoporous NiO–CaO–Al_2O_3 composite oxides for catalyzing CO_2 reforming of CH_4, ACS Catal. 2 (2012) 1331–1342, https://doi.org/10.1021/cs3001072.

[44] G. Agostini, C. Lamberti, R. Pellegrini, G. Leofanti, F. Giannici, A. Longo, E. Groppo, Effect of pre-reduction on the properties and the catalytic activity of Pd/carbon catalysts: a comparison with Pd/Al_2O_3, ACS Catal. 4 (2014) 187–194, https://doi.org/10.1021/cs400507m.

[45] T.W. Hansen, J.B. Wagner, Catalysts under controlled atmospheres in the transmission electron microscope, ACS Catal. 4 (2014) 1673–1685, https://doi.org/10.1021/cs401148d.

[46] A. Joshi, H.S. Zijlstra, S. Collins, J.S. McIndoe, Catalyst deactivation processes during 1-hexene polymerization, ACS Catal. 10 (2020) 7195–7206, https://doi.org/10.1021/acscatal.0c01607.

[47] Z. Benedek, M. Papp, J. Oláh, T. Szilvási, Demonstrating the direct relationship between hydrogen evolution reaction and catalyst deactivation in synthetic Fe nitrogenases, ACS Catal. 10 (2020) 12555–12568, https://doi.org/10.1021/acscatal.0c02315.

[48] M.S. Radue, S. Baek, A. Farzaneh, K.J. Dwyer, Q. Campbell, A.D. Baczewski, E. Bussmann, G.T. Wang, Y. Mo, S. Misra, R.E. Butera, $AlCl_3$-Dosed Si(100)-2 × 1: adsorbates, chlorinated Al chains, and incorporated Al, J. Phys. Chem. C 125 (2021) 11336–11347, https://doi.org/10.1021/acs.jpcc.1c00691.

[49] A.S. Andreev, V.N. Kuznetsov, Y.V. Chizhov, Atomic hydrogen activated TiO_2 nanocluster: DFT calculations, J. Phys. Chem. C 116 (2012) 18139–18145, https://doi.org/10.1021/jp3009805.

[50] R.V. Mom, J. Cheng, M.T.M. Koper, M. Sprik, Modeling the oxygen evolution reaction on metal oxides: the infuence of unrestricted DFT calculations, J. Phys. Chem. C 118 (2014) 4095–4102, https://doi.org/10.1021/jp409373c.

[51] H. Shiiba, N. Zettsu, M. Nakayama, S. Oishi, K. Teshima, Defect formation energy in spinel $LiNi_{0.5}Mn_{1.5}O_{4-\delta}$ using ab initio DFT calculations, J. Phys. Chem. C 119 (2015) 9117–9124, https://doi.org/10.1021/acs.jpcc.5b01661.

[52] M. Delgado, C.C. Santini, F. Delbecq, A. Baudouin, A. De Mallmann, C. Prestipino, S. Norsic, P. Sautet, J.-M. Basset, Characterization of surface hydride hafnium complexes on alumina by a combination of experiments and DFT calculations, J. Phys. Chem. C 115 (2011) 6757–6763, https://doi.org/10.1021/jp200111x.

[53] H. Sun, D. Wu, K. Liu, X. Guo, A. Navrotsky, Energetics of alkali and alkaline earth ion-exchanged zeolite A, J. Phys. Chem. C 120 (2016) 15251–15256, https://doi.org/10.1021/acs.jpcc.6b04840.